Coexistence of 5G with satellite services in the millimeter-wave band

Article (Published Version)

IEEE Access
Multidisciplinary | Rapid Review | Open Access Journal

Received August 13, 2020, accepted August 23, 2020, date of publication September 7, 2020, date of current version September 18, 2020.

Digital Object Identifier 10.1109/ACCESS.2020.3022044

Coexistence of 5G With Satellite Services in the Millimeter-Wave Band

YEONGI CHO[1], (Student Member, IEEE), HYUN-KI KIM[1], (Student Member, IEEE), MAZIAR NEKOVEE[2], AND HAN-SHIN JO[1], (Member, IEEE)

[1]Department of Electronics and Control Engineering, Hanbat National University, Daejeon 34158, South Korea
[2]Department of Engineering and Design, University of Sussex, Brighton BN1 9RH, U.K.

Corresponding author: Han-Shin Jo (hsjo@hanbat.ac.kr)

This work was supported by the research fund of Hanbat National University in 2019.

ABSTRACT In this study, a new method is proposed to confirm the possibility of coexistence between the existing satellite services and potential fifth-generation (5G) cellular services in the millimeter-wave band according to the frequency-designation agenda of International Mobile Telecommunications (IMT)-2020 for 5G. To evaluate the accumulated interference power of numerous 5G systems distributed globally at a satellite receiver, we extend the satellite's interference reception area to the entire coverage area, from which only the land area is extracted using the geospatial terrain data of Earth in three dimensions. This enables more accurate interference assessment than conventional methods that only consider the footprint of the satellite's 3-dB beamwidth. We also place the IMT-2020 (5G) systems in the coverage area using the IMT-2020 parameters and modeling documents for the International Telecommunication Union's coexistence study. The propagation loss is modeled considering the clutter loss, building entry loss, and attenuation from atmospheric gases. Subsequently, we analyze the interference power received by a fixed satellite service (FSS) satellite operating in the same band and an Earth exploration satellite service (EESS) passive sensor operating in an adjacent channel. Our simulation shows that the FSS satellite receives up to 7.9dB more interference than that obtained from the existing method. Although this is a substantial difference, we find that the protection criteria is still satisfied. However, all EESS passive sensors do not meet the protection criteria in most scenarios, and additional frequency separation or interference mitigation techniques are required to protect these sensors. The proposed method is also applicable to the analysis of non-terrestrial network interference from airships, balloons, unmanned aerial vehicles, etc.

INDEX TERMS Coexistence, earth exploration satellite service, fixed satellite service, international mobile telecommunications-2020, non-terrestrial network, radio interference, 5G.

I. INTRODUCTION

A. BACKGROUND AND MOTIVATION

According to a market research report, global mobile data traffic is expected to increase to 49 exabytes (EB) per month by 2021 owing to the increase in the number of smartphone users, the Internet of Things, and real-time streaming [1]. The easiest way to meet the increasing traffic is to use a wide frequency bandwidth. However, it is currently difficult to secure additional frequencies in the International Mobile Telecommunications (IMT) advanced frequency band. The millimeter-wave (mmWave) band has attracted attention as a solution [2]. The radio wave of mmWave band has strong straightness compared to the IMT advanced frequency band due to the short wavelength. Therefore, mmWave propagation loss is large and sensitive to the atmospheric environment, which is a critical disadvantage in mobile communications. However, the mmWave band has a wide bandwidth and can be equipped with more antennas because the antennas can be made smaller and lighter. Therefore, many research institutes have conducted research on beamforming technology to increase antenna gain by using multiple antenna arrays, which is one of the most important technologies resulting from IMT-2020 [3].

In 2015, the World Radiocommunication Conference (WRC-15) adopted WRC-19 Agenda item 1.13 to find an appropriate frequency for 5G IMT-2020 in the mmWave band and presented a total of 11 candidate frequency bands in

The associate editor coordinating the review of this manuscript and approving it for publication was Renato Ferrero.

TABLE 1. International frequency allocation status.

Frequency band	International Frequency Allocation
24.25–27.5 GHz	FS, FSS, RNS (Regions 2 and 3)
31.8–33.4 GHz	FS, RNS, SRS
37–40 GHz	FS, FSS, Mobile, EESS (secondary)
40.5–42.5 GHz	FS, FSS, Mobile (secondary)
42.5–43.5 GHz	Broadcasting satellite, Broadcasting
47–47.2 GHz	Amateur, Amateur satellite
47.2–50.2 GHz	FS, FSS, Mobile
50.4–52.6 GHz	FS, FSS, Mobile
66–71 GHz	Mobile, MSS, RNS, Radio navigation satellite
71–76 GHz	FS, FSS, Mobile, MSS
81–86 GHz	FS, FSS, Mobile, MSS, Radio astronomy

※ SRS: Space research service; EESS: Earth exploration satellite service; RNS: Radio navigation service; FSS: Fixed satellite service; MSS: Mobile satellite service; FS: Fixed service; ISS: Inter-satellite service

※ Region 1: Europe, Africa; Region 2: America; Region 3: Asia, Oceania

the 24.25–86-GHz band [4]. Therefore, to determine the frequency band for IMT-2020, coexistence studies with existing services allocated to candidate bands must be undertaken. Table 1 lists the types of services currently allocated in the candidate bands of IMT-2020. A wide variety of services are allocated to the candidate bands of IMT-2020; therefore, Agenda 1.13 requires very complex coexistence studies on various scenarios compared with the coexistence studies previously conducted by the International Telecommunication Union (ITU).

As shown in Table 1, there are many services using satellites in the candidate band. We thus focus on the coexistence of 5G with fixed satellite service (FSS) and earth exploration satellite service (EESS), based on the parameter and modeling documents of IMT-2020 proposed by the ITU radiocommunication sector (ITU-R) [5], [6].

B. PREVIOUS STUDIES AND CONTRIBUTIONS

Recently, research on the possibility of coexistence between millimeter wave band IMT-2020 candidate technology and other existing radio services has been actively conducted. The cochannel sharing between IMT-2020 and fixed service (FS) systems are studied in [7]–[10]. Jo *et al.* [11] proposed the analytical expression of the frequency-dependent rejection (FDR) of CP-OFDM, windowed OFDM, and filtered OFDM for assessing the interference of IMT-2020 to the incumbent radar systems.

Interference analysis between the IMT and satellite service has already been performed several times [12]–[19]. However, most studies focus on analyzing the interference between the IMT and satellite Earth stations and either postpone or do not address the issue of interference received by satellite systems [12]–[17]. This is because one may expect that because satellite systems are located at high altitudes, interference from the IMT is very small and thus no interference problems occur in satellite systems. However, satellites receive interference aggregated from numerous terrestrial IMT-2020 systems distributed over large areas, and the total inference could be severe for satellite systems that are sensitive to interference. Therefore, to achieve complete coexistence of the two services, interference power received by the existing satellite systems needs to be estimated.

Previous studies analyzing the interference received by satellites in the mmWave band used two methods to calculate the interference. The first method is to calculate the interference power received by a satellite system from a single IMT system and then multiply it by the number of IMTs distributed within the footprint of the satellite's main beam [18]. The other method is to implement a single cell of an IMT network with hexagonal cells, calculate the interference received by the FSS satellites from this network, and find the maximum number of networks that meet the protection criteria [19].

The advantage of these methods is their ability to predict the interference power received from multiple IMT systems in a short time by multiplying the coverage area after considering interference only on IMTs distributed in a single or very small area. However, they also have a limitation that the cumulative interference power received from a very wide range cannot be calculated accurately. The reasons are as follows.

First, the method of distributing only a single IMT or a single IMT network cannot fully consider probabilistic factors of interference power such as antenna orientation, three-dimensional beamforming, and uplink power control. In particular, the mmWave IMT system performs three-dimensional narrow beamforming toward the other end of a transceiver pair to compensate for severe path loss, and accordingly, the interference power generated by the 5G system varies greatly depending on the direction.

Second, the existing methods only consider the footprint, which is the area corresponding to the satellite's 3-dB beamwidth out of the satellite's total interference reception area. This means that the interference received in the area corresponding to the satellite's side lobes is ignored, which can lead to significant differences from the actual interference level. Furthermore, there is no distinction between the land and sea in areas where terrestrial IMT systems are distributed. The IMT systems are distributed over land, and the land area ratio for the interference-receiving area depends on the coordinates where the satellite system is located. Therefore, if the cumulative interference power is calculated by simply multiplying the number of single IMT systems or local

IMT networks, a cumulative interference power error occurs because the sea area, in which the IMT system is not distributed, is included in the interference area.

Third, in a previous study, only free-space path loss (FSPL) and simplified clutter loss were adopted when calculating the propagation loss from IMT systems to a satellite. Propagation loss is among the most influential factors in calculating interference power, and modeling the propagation phenomenon as accurately as possible is essential for interference analysis. In particular, because the mmWave band is sensitive to the atmospheric environment, it is essential to realistically model the propagation phenomenon. However, the propagation-loss model used by existing methods alone does not take into consideration various propagation phenomena occurring in the mmWave band.

To improve upon these weaknesses, the authors perform an initial study to calculate the interference of IMT-2020 at the satellite for FSS using IMT-2020 modeling, propagation loss, and terrain data proposed in ITU-R Recommendation [20], [21]. As in previous studies, interference analysis is only performed with an FSS satellite, but the interference received by the EESS satellite allocated to the adjacent channel by IMT-2020 is not considered.

In this paper, we propose a new method of interference analysis to calculate the interference received from the IMT-2020 by satellite systems.[1] Unlike the conventional method, it calculates the total coverage area where satellites receive interference according to the altitude of the satellite by considering the curvature of the Earth as well as distributes the base station (BS) and user equipment (UE) of IMT-2020 in different environments using the distribution method proposed by ITU-R [22]. Subsequently, using the terrain data and interpolation method, we remove the IMT-2020s distributed in the marine area of the coverage area and perform interference analysis considering only the IMT-2020s distributed in the land area [24], [25]. This allows similar modeling to the situation where satellites actually receive interference from ground-based IMT-2020. We also implement a three-dimensional beamforming pattern, one of the core technologies of IMT-2020, using a newly proposed modeling document for frequency-sharing analysis by ITU-R [6]. Moreover, we apply the propagation-loss model by considering various propagation phenomena occurring in the actual mmWave band, such as clutter loss, building entry loss, and atmospheric loss [26]–[28]. Subsequently, we calculate the interference received by the FSS satellites assigned to the same band and the EESS passive sensors assigned to adjacent bands when the IMT-2020 is operating in the candidate band using the proposed model. Then, the calculated interference power is compared with the protection criteria of each satellite to suggest the possibility of coexistence between IMT-2020 and two satellite services. Finally, we perform interference analysis with more various types of satellite systems, including the results presented in previous papers.

[1] Part of the results were published in recent work [22].

TABLE 2. Key symbols and definitions of interference analysis.

Symbol	Definition
S	Coverage area of satellite
N_{IMT}	# of IMT-2020
A_E	Antenna element gain of IMT-2020
A_{Beam}	Beamforming gain of IMT-2020
PL_{total}	Total propagation loss
PL_{free}	Free-space path loss
L_{clutter}	Clutter loss
L_{building}	Building entry loss
A_{ag}	Attenuation due to atmospheric gases
L_{BS}	Beam spread loss
L_{pol}	Polarization loss
L_{body}	Body loss
G_{SS}	Receiving antenna gain of satellite
OTR	On-tune rejection
I_{single}	Interference power of single IMT-2020
I_{total}	Total interference power
INR_{th}	Protection criteria of satellite in the interference-to-noise ratio format
N	Noise power

In the case of the FSS interference scenario, the interference received by the four types of FSS satellites is assessed. For the EESS passive interference scenario, we calculate the interference received by two types of passive sensors that scan urban or suburban area. In addition, considering the future development of array antenna design technology, we analyze the interference power from the IMT-2020 with more antenna elements as well.

The remainder of this paper is organized as follows. Section II explains how to distribute the IMT-2020s within the satellite's coverage area. Section III describes the radio propagation model applied between the ground and the universe. Section IV describes how to calculate the cumulative interference power received by satellite. Section V and Section VI detail the interference scenarios and simulation results to evaluate the possibility of coexistence with satellite systems and IMT-2020. We conclude the paper in Section VII.

Table 2 describes the key symbols and meanings defined in this study. We considered various variables to perform the interference analysis.

II. IMT-2020 MODELING FOR INTERFERENCE ANALYSIS

A. IMT-2020 DISTRIBUTION OVER THE EARTH'S SURFACE

Fig. 1 shows the interference scenario of the interference-analysis model proposed in this paper. When the satellite service operates uplink in the mmWave band, if IMT-2020 is newly serviced in the same channel or an adjacent channel, the satellite system receives interference from a number of IMT-2020s placed on the land area. To calculate the

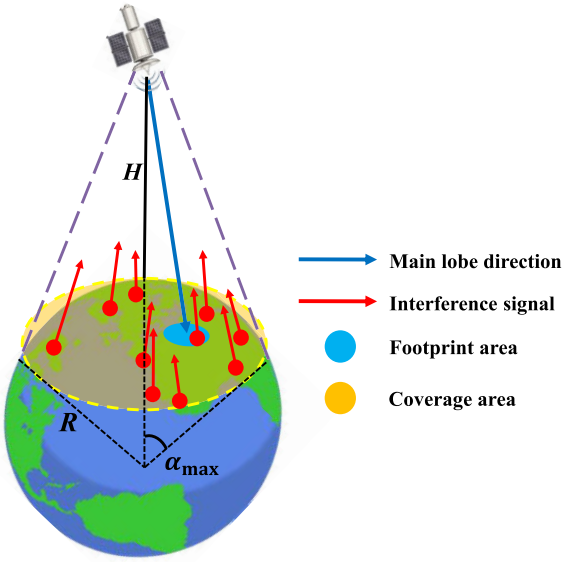

FIGURE 1. Interference scenario that satellite receives from IMT-2020.

interference that the satellite system receives, we first calculate the coverage area of the satellite and distribute the IMT-2020 BS and UE therein. The coverage area S of the satellite is as follows:

$$S = 2\pi R^2 \left[1 - \cos\left(\alpha_{\max}\right)\right], \tag{1}$$

where R is the radius of the Earth and $\alpha_{\max}$ is the central angle between the satellite and the Earth, expressed as

$$\alpha_{\max} = \cos^{-1}\left[R/\left(H + R\right)\right], \tag{2}$$

where H is the orbit of the satellite. After calculating the coverage area, IMT-2020 BS and UE are distributed in the area. The number of IMT-2020s distributed in the satellite coverage area is as follows:

$$N_{\text{IMT}} = S \cdot D \cdot R_a \cdot R_b \cdot F_{\text{NL}} \cdot F_{\text{TDD}}, \tag{3}$$

where S is the coverage area from (1), D is the density of IMT-2020 BSs or UEs, R_a is the ratio of hotspot areas to areas of cities, built-up areas, and districts, R_b is the ratio of built-up areas to the total area of the region, F_{NL} is the network loading factor, and F_{TDD} is the time-division duplexing activity factor [5].

Figs. 2 and 3 show the distribution of IMT-2020 BS and UE. BSs are distributed assuming a uniform distribution within the satellite's coverage area using a spherical coordinate system (R, θ, φ). When the satellite is located at $(R+H, \pi/2, 0)$, the position of the BS is determined by two random variables x_1, x_2, with a uniform distribution between 0 and 1, and is expressed as

$$\begin{aligned} r_{\text{BS}} &= R, \\ \theta_{\text{BS}} &= \pi/2 - \arccos\left\{1 - x_2\left[1 - \cos\left(\left(\alpha_{\max}\right)\right)\right]\right\}, \\ \phi_{\text{BS}} &= \left(2x_1 - 1\right) \cdot \pi. \end{aligned} \tag{4}$$

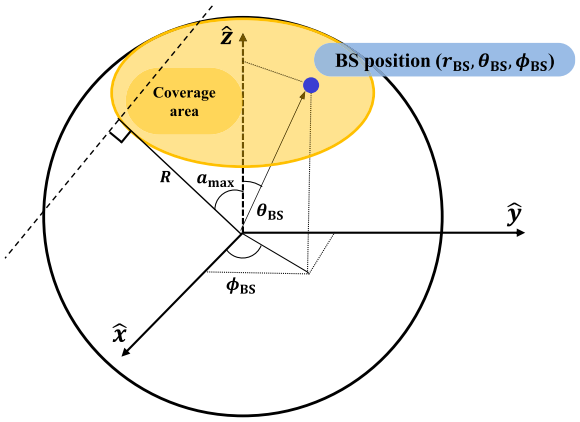

a) Spherical coordinates of distributed BS

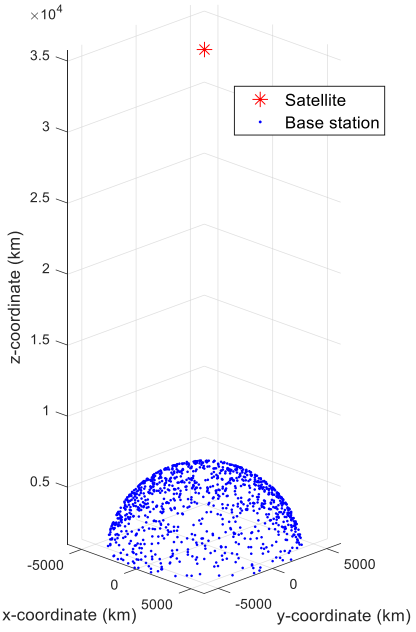

b) IMT-2020s distributed in the coverage area according to the orbit of the satellite

FIGURE 2. Base station distribution.

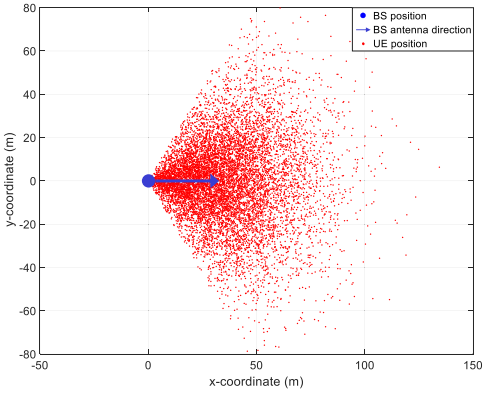

FIGURE 3. User equipment distribution.

The antenna direction of the BS is determined as a random direction in the azimuth and has an additional 10° mechanical downtilt [22]. The distribution of the UE is

determined by the BS position and the antenna direction. First, the virtual BS communication with the UE is distributed and given the antenna direction of the BS. Then, as shown in Fig. 3, it is distributed between ± 60° in the azimuth direction based on the antenna direction of the BS. The distance from the BS follows the Rayleigh distribution [22]. The antenna direction of the UE is determined in a random direction in the azimuth. The BSs all assume an outdoor environment, and in the case of the UE, an outdoor or indoor environment is assumed according to a given probability.

B. IMT-2020 SAMPLING USING TERRAIN DATA

In this study, we extended the coverage area of the satellite to the entire area, accounting for the satellite's side lobes, and distributed IMT-2020s within it. However, in this case, because there is no distinction between land and sea, a problem arises in that IMT-2020, which should be distributed only on land, is also distributed in the sea region. This allows the satellite to receive interference from more IMT-2020s than it actually does; therefore, using this assumption does not allow for calculation of the exact cumulative interference power. To solve this problem, we adopted a method that considers only IMT-2020 distributed over land area according to the position of satellites using map data and interpolation [23], [24].

As shown in Fig. 2, IMT-2020 BSs are placed assuming that the satellite is located on the z axis. This is because when the satellite is located on the z axis while IMT-2020 is distributed within the satellite's coverage area using the spherical coordinate system, ϕ can be set easily to a value with a uniform distribution between -π and π. Thus, we could easily distribute the IMT-2020s on the Earth's surface. However, we do not know the latitude and longitude of IMT-2020s located in the coverage area according to the geographical location of the satellite. Therefore, to use the sampling, we use a coordinate transformation and a rotation matrix to move the distributed IMT-2020s to the satellite's coverage area according to the coordinates of the satellite's geographic location.

First, we transform the distributed IMT-2020s from a spherical coordinate system to a Cartesian coordinate system through a coordinate transformation. Then, using the rotation matrix, we rotate the distributed IMT-2020s 90° clockwise about the y axis and convert them back to the spherical coordinate system through the coordinate system transformation matrix. In this case, the azimuth and elevation of IMT-2020 is composed of a spherical coordinate system that represents longitude and latitude coordinates of the IMT-2020 present in the coverage area when the satellite's longitude and latitude are origin. Finally, we set the coordinates of IMT-2020 distributed in the satellite's coverage area by shifting the azimuth and elevation angles of IMT-2020 positions by the latitude and longitude of the satellite. This process can be

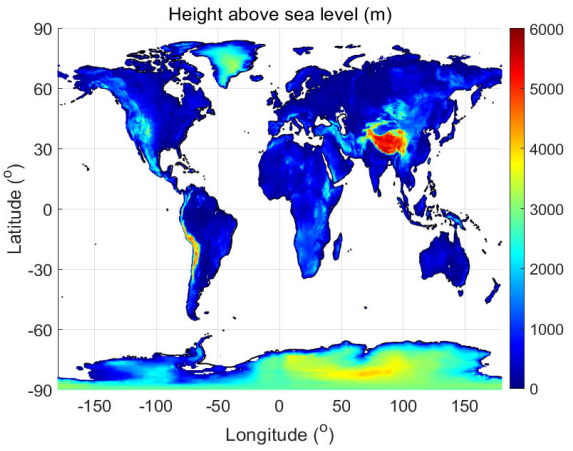

FIGURE 4. Terrain height data of Earth [18].

expressed as

$$\begin{pmatrix} r_{\mathrm{IMT}} \\ \theta_{\mathrm{Lat}} \\ \phi_{\mathrm{Lon}} \end{pmatrix} = \left[\mathbf{A} \times \mathbf{B} \times \mathbf{A}^{-1} \times \begin{pmatrix} r_{\mathrm{IMT}} \\ \theta_{\mathrm{IMT}} \\ \phi_{\mathrm{IMT}} \end{pmatrix} \right] + \begin{pmatrix} 0 \\ \mathrm{Lat}_{\mathrm{Sat}} \\ \mathrm{Lon}_{\mathrm{Sat}} \end{pmatrix},$$

$$\mathbf{A} = \begin{pmatrix} \sin\theta_{\mathrm{IMT}} \cos\phi_{\mathrm{IMT}} & \sin\theta_{\mathrm{IMT}} \sin\phi_{\mathrm{IMT}} & \cos\theta_{\mathrm{IMT}} \\ \cos\theta_{\mathrm{IMT}} \cos\phi_{\mathrm{IMT}} & \cos\theta_{\mathrm{IMT}} \sin\phi_{\mathrm{IMT}} & -\sin\theta_{\mathrm{IMT}} \\ -\sin\phi_{\mathrm{IMT}} & \cos\phi_{\mathrm{IMT}} & 0 \end{pmatrix},$$

$$\mathbf{B} = \begin{pmatrix} 0 & 0 & -1 \\ 0 & 1 & 0 \\ 1 & 0 & 0 \end{pmatrix}, \quad (5)$$

where $\mathbf{A}$ is a transform matrix that converts a Cartesian coordinate system to a spherical coordinate system, and $\mathbf{B}$ is a rotation matrix that rotates the coordinates 90° clockwise about the y axis. r_{IMT}, θ_{IMT}, and ϕ_{IMT} are the spherical coordinates of IMT-2020s and $\mathrm{Lat}_{\mathrm{sat}}$ and $\mathrm{Lon}_{\mathrm{sat}}$ are the latitude and longitude of the satellite, respectively.

Then, we sample the IMT-2020s using terrain data and an interpolation method. Fig. 4 shows the height above sea level (HASL) at the latitude and longitude coordinates using the terrain data provided by ITU-R P.836. The HASL is given at 0.5° intervals, and the values in between 0.5 degree are calculated by the interpolation methods described in ITU-R P.1144: bi-linear interpolation using 4 grid points and bi-cubic interpolation using 16 grid points. The bi-cubic interpolation is able to estimate the HSAL value for more locations among the given coordinates, whereas the bi-linear interpolation simple and exact enough to only differentiate land area from the entire coverage area. Therefore, a simple bi-linear interpolation method is used to calculate the HASL in the region where each IMT-2020 is located. The HASL of the IMT-2020 is calculated using the grid points [(Lat_0, Lon_0), (Lat_1, Lon_0), (Lat_0, Lon_1), and (Lat_1, Lon_1)] closest to the coordinates of the IMT-2020 in the given terrain data,

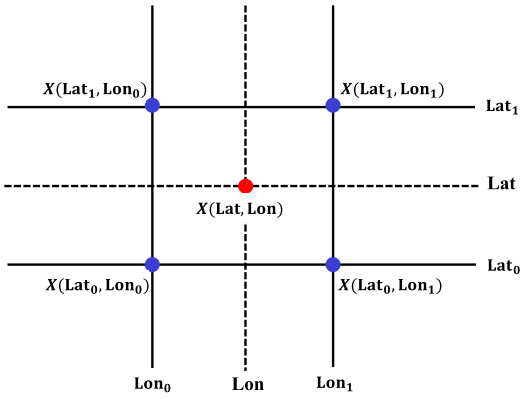

FIGURE 5. Interpolation grid points [19].

as shown in Fig. 5. When IMT-2020 is located at (Lat, Lon), the HASL X (Lat, Lon) of IMT-2020 is given as

$$\begin{aligned} X\,(\mathrm{Lat}, \mathrm{Lon}) = {} & (1-s)\,(1-t)\,X\,(\mathrm{Lat}_0, \mathrm{Lon}_0) \\ & + (1-s)\,t\,X\,(\mathrm{Lat}_1, \mathrm{Lon}_0) \\ & + s\,(1-t)\,X\,(\mathrm{Lat}_0, \mathrm{Lon}_1) \\ & + t\,s\,X\,(\mathrm{Lat}_0, \mathrm{Lon}_1)\,, \end{aligned} \tag{6}$$

where s and t are given by

$$s = \frac{\mathrm{Lon} - \mathrm{Lon}_0}{\mathrm{Lon}_1 - \mathrm{Lon}_0}, \tag{7}$$

$$t = \frac{Lat - Lat_0}{Lat_1 - Lat_0}. \tag{8}$$

We calculate the HASL according to the position of IMT-2020 distributed in the coverage area and remove the IMT-2020 where the HASL is zero. Thus, we can perform more accurate interference analysis by considering only the land areas present within the coverage area of the satellite system.

C. IMT-2020 ANTENNA MODELING

In this paper, we assumed that the IMT-2020 used the mmWave band we consider a potential IMT-2020 system in mmWave band. The mmWave has a fatal disadvantage for wireless communication: it has high straightness due to the short wavelength, which is the cause of high path loss and atmospheric loss. To compensate for these drawbacks, IMT-2020 uses the advantage of antenna miniaturization to improve the directivity between communication links through three-dimensional beamforming technology using multiple antenna arrays.

The transmitting antenna gain of the IMT-2020 is calculated as the sum of the antenna element gain and the beamforming gain. The antenna element gain is determined by the azimuth and elevation angles between the antenna's main beam direction of IMT-2020 and that of the satellites and is given by

$$A_E\,(\varphi, \theta) = G_{E,\max} - \min\left\{-\left[A_{E,H}\,(\varphi) + A_{E,v}\,(\theta)\right], A_m\right\}\,, \tag{9}$$

where $G_{E,\max}$ is the maximum antenna element gain of IMT-2020, $A_{E,H}\,(\varphi)$ and $A_{E,V}\,(\theta)$ are the antenna radiation patterns in the horizontal and vertical directions, respectively, and A_m is the front to back ratio of horizontal and vertical parameters. $A_{E,H}\,(\varphi)$ and $A_{E,V}\,(\theta)$ are expressed as

$$A_{E,H}\,(\varphi) = -\min\left[12\left(\frac{\varphi}{\varphi_{3dB}}\right)^2, A_m\right], \tag{10}$$

$$A_{E,V}\,(\varphi) = -\min\left[12\left(\frac{\theta - 90}{\theta_{3dB}}\right)^2, SLA_v\right], \tag{11}$$

where $\varphi_{3\,\mathrm{dB}}$ and $\theta_{3\mathrm{dB}}$ are the 3-dB beamwidths of the horizontal and vertical patterns, respectively [6].

The antenna array of IMT-2020 is $N_H \times N_V$ and the beamforming gain is calculated as

$$A_{\mathrm{Beam}}\,(\varphi, \theta) = 10\log_{10}\left(\left|\sum_{m=1}^{N_H}\sum_{n=1}^{N_V} w_{n,m}\cdot v_{n,m}\right|^2\right), \tag{12}$$

where v is the superposition vector and w is the beamforming weight. Here, v and w are represented as

$$v_{n,m} = \exp\left\{j\cdot 2\pi\left[\begin{array}{l}(n-1)\cdot\dfrac{d}{\lambda}\cdot\cos(\theta) \\ +(m-1)\cdot\dfrac{d}{\lambda}\cdot\sin(\theta)\sin(\varphi)\end{array}\right]\right\}, \tag{13}$$

$$W_{n,m} = \frac{1}{\sqrt{N_H\cdot N_V}} \times \exp\left\{j\cdot 2\pi\left[\begin{array}{l}(n-1)\cdot\dfrac{d}{\lambda}\cdot\sin(\theta_{\mathrm{etilt}}) \\ -(m-1)\cdot\dfrac{d}{\lambda}\cdot\cos(\theta_{\mathrm{etilt}})\sin(\varphi_{\mathrm{escan}})\end{array}\right]\right\}, \tag{14}$$

where d, λ, $\varphi_{i,\mathrm{escan}}$ and $\theta_{\mathrm{i,etilt}}$ are the radiating element spacing, wavelength, horizontal and vertical angles between the antenna direction of IMT-2020 and the direction of beamforming [6].

Fig. 6 shows the single-element antenna pattern of IMT-2020, and Fig. 7 shows the beamforming pattern of IMT-2020 for 4×4, 8×8, and 16×16 antenna arrays. In Fig. 7, as the number of antenna elements increases, higher antenna directivity is obtained; the gain in the main beam direction increases, whereas the gain in the side lobes decreases. Using (9)–(14), we calculate the transmitting antenna gain of IMT-2020 to the satellite direction according to the antenna and beamforming direction of the distributed IMT-2020.

III. PROPAGATION-LOSS MODEL

The total propagation loss between the IMT-2020 and the satellite system is calculated by considering the losses due to various propagation environments between the Earth and space. The total propagation loss occurs when the interfering signal of IMT-2020 reaches the satellite system is expressed

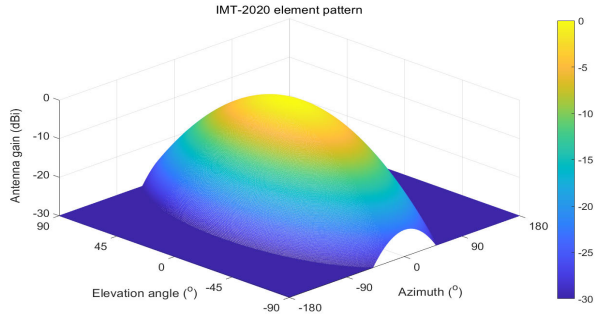

FIGURE 6. Element antenna pattern of IMT-2020.

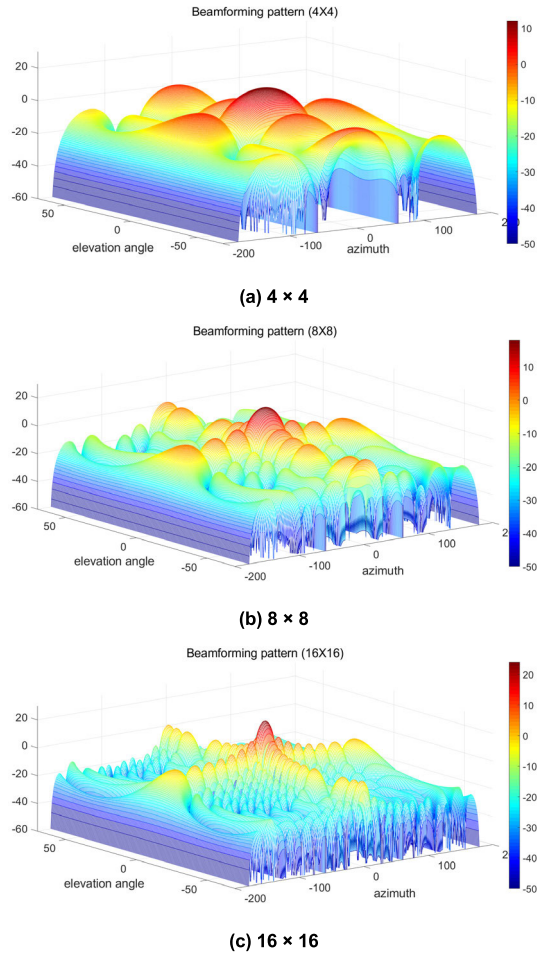

(a) 4 × 4

(b) 8 × 8

(c) 16 × 16

FIGURE 7. Beamforming pattern of IMT-2020 according to the antenna array.

as

$$PL_{\text{total}} = PL_{\text{free}} + L_{\text{clutter}} + L_{\text{building}} + A_{\text{ag}} + L_{\text{BS}} + L_{\text{pol}} + L_{\text{body}}, \quad (15)$$

where PL_{free}, L_{clutter}, L_{building}, A_{ag}, L_{bs}, L_{pol}, and L_{body} are the FSPL, clutter loss [26], building entry loss [27], attenuation due to atmospheric gases [28], beam spread loss, polarization loss, and body loss, respectively.

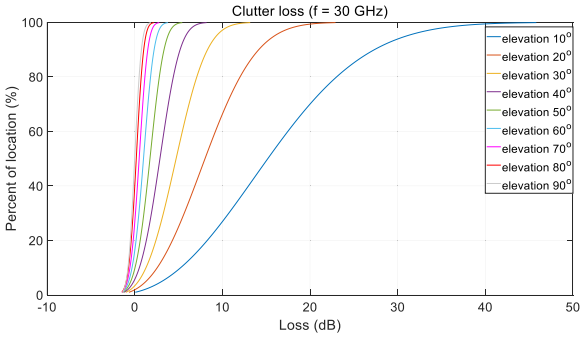

FIGURE 8. Clutter loss ($f = 30$ GHz).

A. FREE-SPACE PATH LOSS

FSPL is used to predict the strength of the received signal in a line-of-sight (LOS) environment, where there are no obstacles between the transmitting and receiving stations. Because most of the paths from IMT-2020 to satellites are free space, the total propagation loss is calculated by adding the propagation loss from the Earth based on the FSPL. If the distance is d km and the frequency is f GHz, it can be expressed as

$$PL_{\text{free}} = 20\log_{10}(f \cdot d) + 92.45 \text{ [dB]}. \quad (16)$$

B. CLUTTER LOSS (ITU-R P.2108)

The ITU-R P.2108 [26] describes clutter as obstacles such as ground buildings or vegetation. Normally, clutter close to the receiving terminal has a strong influence on propagation, but clutter distance is affected by the characteristics of the clutter and the propagation parameters. P.2108 proposes a method to calculate clutter loss in the ground path and the Earth-to-space path for 10–100 GHz. In this paper, the clutter-loss model that occurs in the Earth-to-space path is used. When the elevation angle is θ in the path between IMT-2020 and the satellite and the percentage of location does not exceed $p\%$, clutter loss is given by

$$L_{\text{clutter}} = \left\{-93\left(f^{0.175}\right)\left[\ln\left(1-\frac{p}{100}\right)\right]\cdot \cot\left[0.05\left(1-\frac{\theta}{90}\right)+\frac{\pi\theta}{180}\right]\right\}^{[0.5(90-\theta)/90]} - 1 - 0.6Q^{-1}\left(\frac{p}{100}\right) \text{ [dB]}, \quad (17)$$

where $Q^{-1}\left(\frac{p}{100}\right)$ is the inverse complementary normal distribution function. Fig. 8 shows the clutter loss at 30 GHz according to the elevation angle and percentage of the location, where the clutter loss increases as the elevation angle decreases and the percentage of the location increases. In this study, θ is determined by the distribution of IMT-2020 and the satellite position, and p assumes that all IMT-2020s have random values between 0 and 100%.

C. BUILDING ENTRY LOSS (ITU-R P.2109)

If the IMT-2020 is deployed in an indoor environment, the loss incurred as the signal passes through the building walls

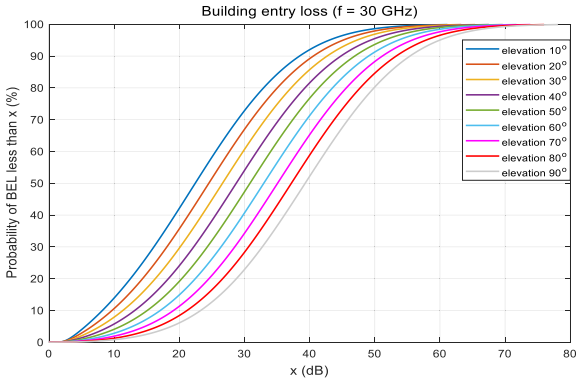

FIGURE 9. Building entry loss (f = 30 GHz).

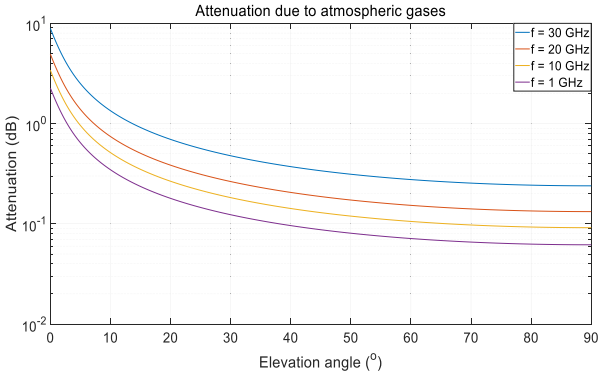

FIGURE 10. Attenuation by atmospheric gases.

should be considered. ITU-R P.2019 [27] provides a model for building entry loss. In general, it is necessary to use various building data, such as the wall thickness, the medium, and so on, to calculate the building entry loss. However, characterizing different types of buildings is not appropriate for general applications, such as spectral sharing studies, because it requires many data and computations. Therefore, the P.2019 document proposed a model for calculating probability-induced building penetration losses in the range from 0.08 to 100 GHz, based on the measurement data collected from Report ITU-R P.2346 [29], which is expressed as

$$L_{\text{building}} = 10\log_{10}\left(10^{0.1A(P)} + 10^{0.1B(P)} + 10^{-0.3}\right) \text{ [dB]}, \tag{18}$$

where $A(P)$ and $B(P)$ are given as

$$\begin{aligned} A(P) &= F^{-1}(P)\,\sigma_1 + \mu_1 \\ B(P) &= F^{-1}(P)\,\sigma_2 + \mu_2, \end{aligned} \tag{19}$$

where P and $F^{-1}(P)$ are the probability that a certain loss is not exceeded ($0\ \% < P < 100\ \%$) and the inverse cumulative normal distribution as a function of probability. Furthermore, σ_1, σ_2, μ_1, and μ_2 are given in the ITU-R P.2109 document and include the median loss for horizontal paths, correction for the elevation angle of the path at the building facade, and variables according to the building type. Fig. 9 shows the building entry loss according to P and the elevation angle when the frequency is 30 GHz. The building entry loss is applied only to the IMT-2020 deployed in indoor environments, and the building penetration loss is calculated using a random P value between 0 and 100%.

D. ATTENUATION DUE TO ATMOSPHERIC GASES (ITU-R P.619)

In (15), A_{ag} stands for the attenuation due to absorption by atmospheric gases such as oxygen, water vapor, and carbon monoxide. The higher the frequency of the signal, the more it is affected by atmospheric gases. In addition, the attenuation increases as the path elevation angle decreases due to the longer path in the atmosphere.

ITU-R P.619 Attachment C to Annex 1 proposes a model for power attenuation due to atmospheric gases [28]. This model calculates atmospheric losses by considering various variables, such as HASL, IMT-2020 antenna height, elevation angle, water vapor volume, air pressure, and temperature. Fig. 10 shows the attenuation due to absorption by atmospheric gases according to the frequency and elevation angle if the vapor density is 7.5 g/m^3 and the altitude is 1 km above sea level. This shows that the higher the frequency band and the lower the elevation angle, the greater the attenuation of the signal by atmospheric gases.

E. OTHER LOSSES

In addition to the four propagation losses described above, we also considered beam spread loss, polarization loss, and body loss. Beam spread loss L_{bs} is represented as

$$L_{\text{spread}} = \pm 10\log_{10}(B), \tag{20}$$

where B is given in [28] and depends on the value of the elevation angle. Polarization loss L_{pol} and body loss L_{body} are assumed to be constants, and 3 dB and 4 dB are also considered. In the case of L_{pol}, the same applies to all IMT-2020s. However, L_{body} only applies to the UEs because it represents the loss of the UE signal passing through the body [5].

IV. INTERFERENCE POWER CALCULATION

The interference power received by the satellite from the ith IMT-2020 is calculated as follows:

$$\begin{aligned} I_{\text{single},i} = P_{t,i} + G_{\text{IMT},i}\left(\phi_i,\ \phi_{i,\text{scan}},\ \theta_i,\ \theta_{i,tilt}\right) \\ - PL_{\text{total},i} + G_{\text{SS},i}(\psi) - \text{OTR}, \end{aligned} \tag{21}$$

where P_t, G_{IMT}, PL_{total}, G_{SS}, and OTR are the transmitting power of the IMT-2020, transmitting antenna gain of IMT-2020 introduced in Section II, total propagation loss introduced in Section III, receiving antenna gain of the satellite, and on-tune rejection (OTR), respectively.

We apply the power control algorithm of UE and the unwanted emission pattern of IMT-2020 to determine Pt.

We assumed a fixed maximum power of the BS. However, the UE adjusts its transmission power through a power control algorithm according to the environment with the serving BS [6]. The power control algorithm of UE is given as

$$P_{\mathrm{UE}} = \min\left(P_m, 10\log_{10}(M_{\mathrm{RB}}) + P_{\mathrm{RB}} + F_{\mathrm{bal}} \cdot CL\right), \quad (22)$$

where P_m is the maximum transmitting power of UE. M_{RB} and P_{RB} are the number of allocated resource blocks (RBs) and the transmitting power per RB, repsectively. F_{bal} is the balancing factor for UEs with bad or good channels, and CL is the coupling loss in dB for the UE from its serving BS, given as [30]

$$\mathrm{CL} = G_{\mathrm{BS}} + G_{\mathrm{UE}} - \mathrm{PL}_{\mathrm{IMT}}, \quad (23)$$

where G_{BS}, G_{UE}, and $\mathrm{PL}_{\mathrm{IMT}}$ are the receiving antenna's gain of BS, transmitting antenna's gain of UE, and path loss between BS and UE. Note that the antenna gain in G_{BS} and G_{UE} indicates the antenna gain in the communication link.

Because the IMT-2020 performs beamforming in the direction of the communicating system, the beamforming gain is assumed to be maximum when calculating G_{BS} and G_{UE}. $\mathrm{PL}_{\mathrm{IMT}}$ is calculated using the modeling document proposed by 3rd generation partnership project (3GPP) [30]. This document describes the physical layer modeling method of the IMT-2020, and we determine the LOS or NLOS channel stochastically according to the distance between the BS and the UE and calculate the path loss accordingly.

In addition, if IMT-2020 and the satellite systems are operated on the same channel, the satellite system receives the complete interference from IMT-2020. However, if both services operate on adjacent channels, we used the unwanted emission mask of IMT-2020 to determine the transmitting power of the IMT-2020 that the satellite system receives. Therefore, we calculate the emission level of IMT-2020 according to the carrier frequency of IMT-2020 and the frequency separation from the satellite system and applied to P_t. IMT-2020's unwanted emission mask depends on IMT-2020's service band and is presented in the ITU Recommendation [5].

The antenna gain G_{SS} received by the satellite is determined by the orbit, maximum gain, 3dB beamwidth, antenna model of the satellite system, off-axis angle Ψ between the main beam direction of the satellite and IMT-2020, etc. ITU proposed various satellite parameters and antenna models for spectrum sharing research. Therefore, we calculate GSS by applying the appropriate parameters and models, depending on the type of satellite that performs the interference analysis. In the following section of this paper, we use the proposed interference-analysis method to calculate the interference power received by the FSS satellite and the EESS passive sensor. To calculate the GSS of the FSS satellite and the EESS passive sensor, we adopted the parameters and antenna model of the FSS satellite and the EESS passive sensor proposed by ITU-R, and more details are described in each chapter.

OTR is the rate of decrease in transmit power owing to the difference between the bandwidth of the transmitting and receiving system. When the receiver bandwidth is greater than or equal to the transmitter bandwidth, the receiver receives the transmission power of the transmitter completely. In the opposite case, however, the transmit power is reduced by the ratio of the transmitter bandwidth to the receiver bandwidth, as the transmit power received outside the receiver's bandwidth is ignored. Therefore, OTR is expressed as (24) when the transmitter bandwidth is B_T, and receiver bandwidth is B_R [31], [32].

$$OTR = \begin{cases} 0, & for\ B_T \le B_R \\ 10\log_{10}\dfrac{B_T}{B_R}, & for\ B_T > B_R \end{cases} \quad (24)$$

We calculate the total received interference power by aggregating all of the IMT-2020 individual interferences. The interference is expressed as

$$I_{total} = 10\log_{10}\left(\sum_{i=1}^{N_{IMT}} 10^{(I_{\mathrm{single},i}/10)}\right). \quad (25)$$

V. INTERFERENCE ANALYSIS BETWEEN IMT-2020 AND SATELLITE SERVICES

In this section, we use the interference-analysis model proposed earlier to perform interference analysis with existing satellite services allocated to the same or adjacent bands when IMT-2020 is serviced in a candidate band. IMT- 2020 is modeled using the parameters in Table 3 and simulations are performed by applying parameters and antenna patterns for each satellite.

A. INTERFERENCE SCENARIO BETWEEN IMT-2020 AND FSS SATELLITE

FSS satellites always operate in a fixed position because they move at the same speed as the Earth's rotational speed. The FSS uplink is currently allocated to the 24.25–27.5 GHz band and the 81–86 GHz band, which is identical to the candidate band of the IMT-2020. Therefore, in order for the IMT-2020 to operate in the candidate band, it is necessary to confirm that the FSS satellite is safe from interference from the IMT-2020 to protect the existing allocated service. FSS satellites are located at a high orbit. Therefore, they have a large coverage area, so they receive the interference power from the IMT-2020 in both urban and suburban areas.

However, because we cannot distinguish between urban and suburban areas, we assumed a uniform distribution in the coverage area of the satellite after adding the total number of IMT-2020s distributed in the urban and suburban areas. Table 4 shows the parameters of the FSS satellites [33]. The IMT-2020 and FSS satellites operate in the same band. Therefore, when calculating the interference power, the satellite

TABLE 3. IMT-2020 parameters [5].

Parameters [Unit]	Value	
	Base station	User equipment
Carrier frequency [GHz]	24.25–27.5, 81–86	
Bandwidth [MHz]	200	
Antenna height [m]	6	1.5
Density/km^2	Urban: 30 Suburban: 10	Urban: 100 Suburban: 30
Resident area ratio [%]	5	
Hotspot area ratio [%]	Urban: 7, Suburban: 3	
Network loading factor [%]	20, 50	
TDD activity factor	80	20
Environment ratio [%]	Outdoor: 100	Outdoor: 80 Indoor: 20
Conducted power [dBm]	10 (27 GHz), 6 (81 GHz)	
Mechanical downtilt [°]	10	-
Peak element antenna gain	5	
Antenna array [$N_H \times N_V$]	8 × 8 (24.25–27.5 GHz) 16 × 16 (81–86 GHz)	4 × 4 (24.25–27.5 GHz) 8 × 4 (81–86 GHz)
3 dB beamwidth [°]	65	90
A_m	30	25
Ohmic loss	3	
Body loss	-	4

TABLE 4. FSS satellite parameters [33].

Parameter [Unit]	Value			
Carrier number	#06	#08	#13	#18
Frequency [GHz]	27–27.5			81–86
Orbit altitude [km]	35,786			8,500
Bandwidth [MHz]	200	200	100	500
Peak receive antenna gain [dBi]	51	45	46.6	64.3
3dB beamwidth [°]	0.65	0.9	0.8	0.11
Ls [dB]	−20	−20	−25	−25
System receive noise temperature [K]	950	950	400	700
Interference protection criteria INR_{th} [dB]	−12.2 [35]			

receives the full interference power of the IMT-2020 without attenuation of the transmission power by the unwanted emission mask.

In (21), to calculate the interference power, G_{SS} represents the receiving antenna's gain of the FSS satellite. We adopted

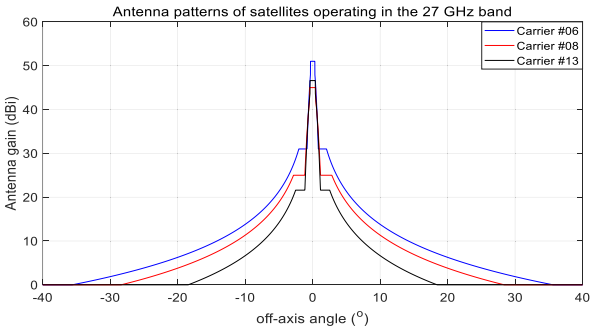

(a) Carrier #06, #08, #13

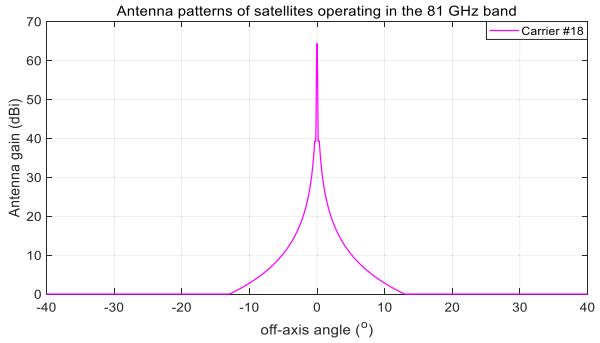

(b) Carrier #18

FIGURE 11. Antenna pattern of FSS satellites.

the antenna model of the FSS satellite proposed by the ITU-R to calculate G_{SS}, which is given by [34]

$$G_{SS}(\psi) = \begin{cases} G_{\max} - 3\,(\psi/\psi_0)^2, & (\psi_0 \le \psi \le a\,\psi_0) \\ G_{\max} + L_0, & (a\,\psi_0 \le \psi \le b\,\psi_0) \\ G_{\max} + L_0 + 20 & \\ \quad -25\log(\psi/\psi_0), & (b\,\psi_0 \le \psi \le \psi_1) \\ 0, & (\psi_1 \le \psi), \end{cases} \tag{26}$$

where $G_{\max}$, ψ_0, ψ_1, and L_o are the maximum gain in the main lobe, 3-dB beamwidth, value of ψ when $G(\psi\ )$ in (26) is equal to 0 dBi, and the required near-in-side-lobe lever (dB) relative to the peak gain. a and b are given in the references as constant values determined by L_o [33]. Fig. 11 shows the antenna pattern of each satellite system according to the off-axis angle. The antenna pattern for Carrier #18 satellites has a higher maximum antenna gain and is sharper than other antenna patterns. This is to compensate for the high propagation loss caused by using higher frequency bands. When performing the simulation, we assumed that all the satellites were located at 9° E. furthermore, the main beam directions are (50° E 45° N), (36.6° E 53.6° N), (50° W 10° S), and (75° E 45° N) for satellites operated in the 27-GHz band, and (50° E 45° N), (36.6° E 53.6° N), and (50° W 10° S), for satellites operated in the 81-GHz band.

Figs. 12 and 13 show the receiving antenna's gain of the satellite along the main beam direction of both satellite systems. In these figures, the orbits of Carriers #06, #08,

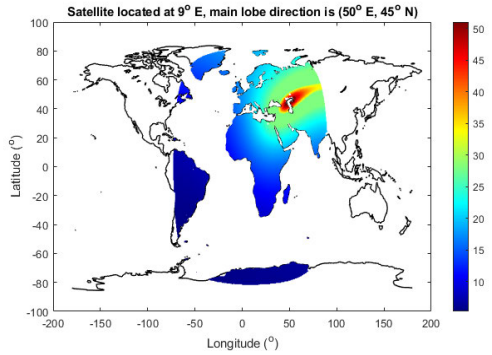

(a) Main beam direction: (50° E, 45° N)

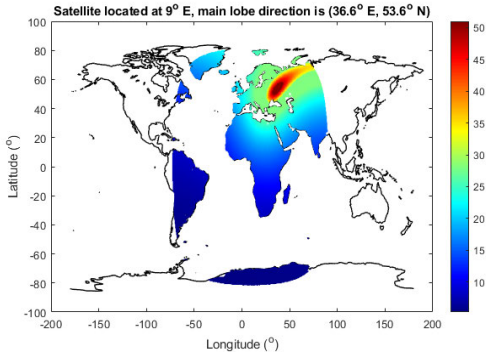

(b) Main beam direction: (36.6° E, 53.6° N)

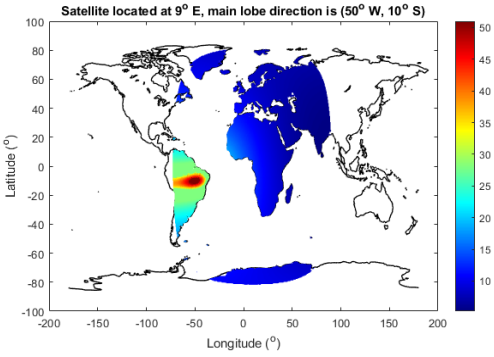

(c) Main beam direction: (50° W, 10° S)

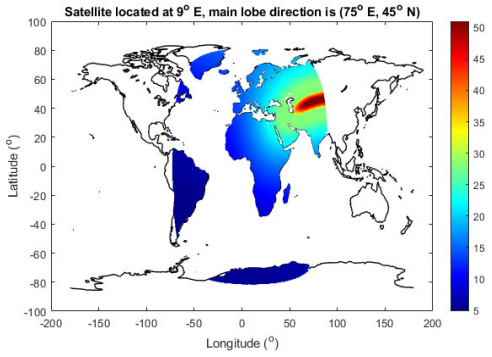

(d) Main beam direction: (75° E, 45° N)

FIGURE 12. Receive antenna gain according to position and main lobe direction of Carrier #06 satellite.

and #13 and satellites #08 and #13 have larger coverage areas than that of Carrier #08. In this case, the number of IMT-2020s is about 1,518,000 for the satellites of Carriers #06,

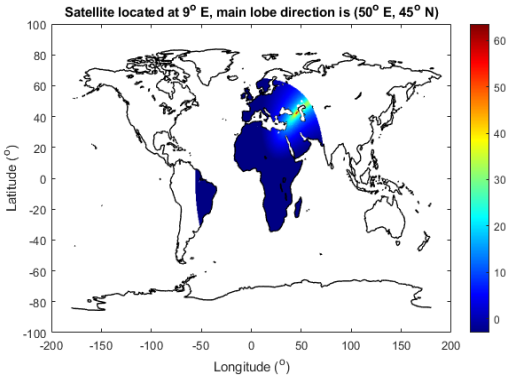

(a) Main beam direction: (50° E, 45° N)

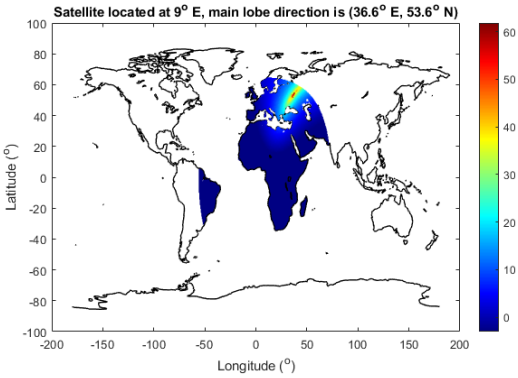

(b) Main beam direction: (36.6° E, 53.6° N)

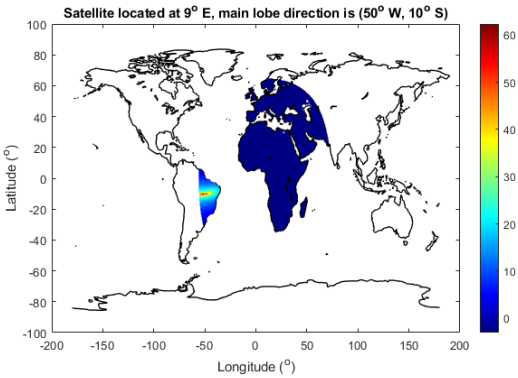

(c) Main beam direction: (50° W, 10° S)

FIGURE 13. Receive antenna gain according to position and main lobe direction of Carrier #18 satellite.

#08, and #13 and 980,000 for the Carrier #18 satellite. In addition, satellites operating in the 27-GHz band have a larger footprint because the beamwidth is wider than that of Carrier #18. However, Carrier #18 satellites have a higher maximum antenna gain than satellites operating in the 27-GHz band. Therefore, Carrier #18 satellites receive much more interference in the footprint than satellites operating in the 27-GHz band. The overall interference power is also highly dependent on the interference received in the footprint.

After calculating the interference power received from each IMT-2020, we calculate the cumulative interference power received by a satellite according to (25) and compare that with the protection criteria to determine the possibility

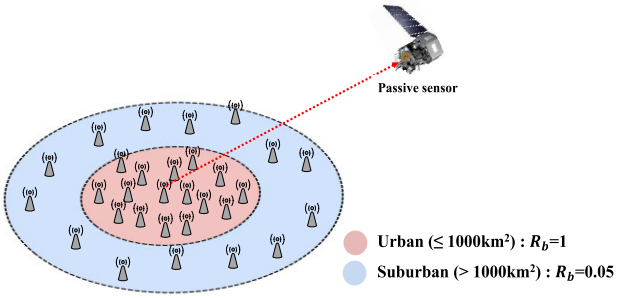

FIGURE 14. IMT-2020 distribution when the sensor scans urban area.

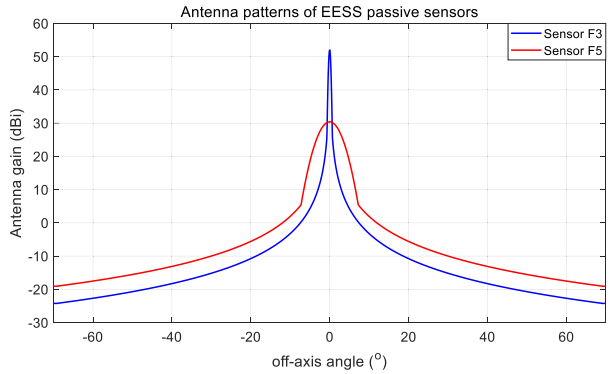

FIGURE 15. Antenna pattern of EESS passive sensors.

of coexistence. According to the ITU-R document on protection criteria, the protection criteria for FSS satellite are presented in the form of an interference-to-noise ratio (INR) [35]. Therefore, the interference power allowance criterion of the satellite system is expressed as

$$I_{\text{th}} = \text{INR}_{\text{th}} + N, \tag{27}$$

where N is the noise of the satellite and is given as

$$N = 10 \log_{10} (k \cdot T \cdot \text{BW}_V), \tag{28}$$

where k, T, and BW_V are the Boltzmann constant, noise temperature, and bandwidth of the satellite system, respectively.

B. INTERFERENCE SCENARIO BETWEEN IMT-2020 AND EESS PASSIVE

EESS is a wireless communication service defined in the ITU-R and is one of the low-Earth orbit (LEO) satellites operating in orbit of about 800 km. Its main purpose is to monitor the condition of the Earth and the atmosphere, and it carries active and passive sensors. Among them, the passive sensor is a receive-only service in which information is obtained by the reception of radio waves of natural origin such as terrain, air pressure, and temperature. It is very sensitive to interference because it receives weak radio waves of natural origin [36].

EESS passive service is currently allocated in the 23.6–24 GHz band, which is adjacent to the 24.25–27.5 GHz band, one of the candidate bands of IMT-2020. Therefore,

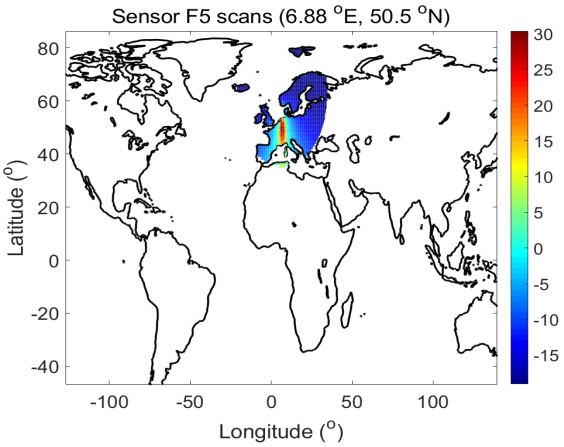

(a) Main beam direction: Germany (6.88° E, 50.5° N)

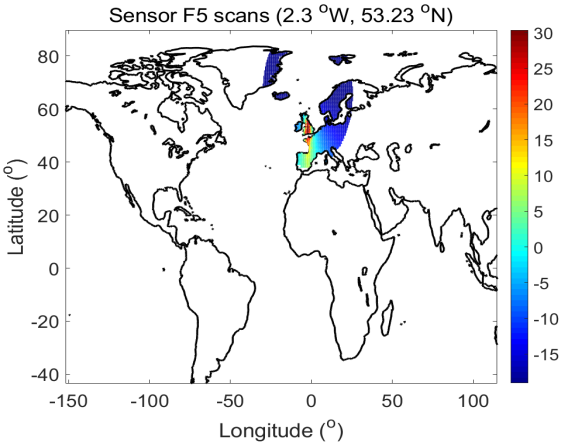

(b) Main beam direction: United Kingdom (2.3° W, 53.23° N)

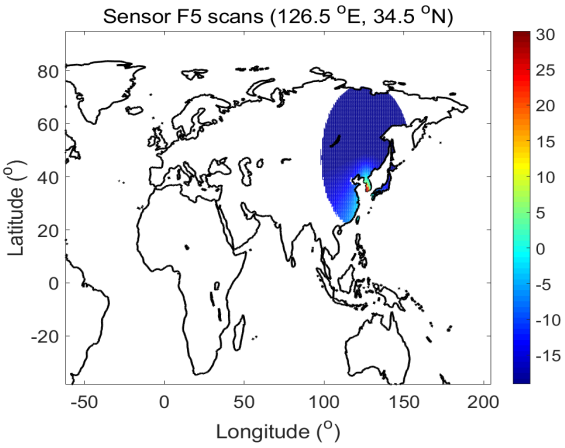

(c) Main beam direction: Korea (126.5° E, 34.5° N)

FIGURE 16. Receive antenna gain of EESS passive sensor according to main lobe direction.

we need interference analysis between IMT-2020 and EESS passive to confirm whether EESS passive can be protected from IMT-2020 operating in the adjacent channels.

In the case of EESS passive, it collects information according to a certain path. Thus, it receives interference from IMT-2020 deployed in various environments such as rural,

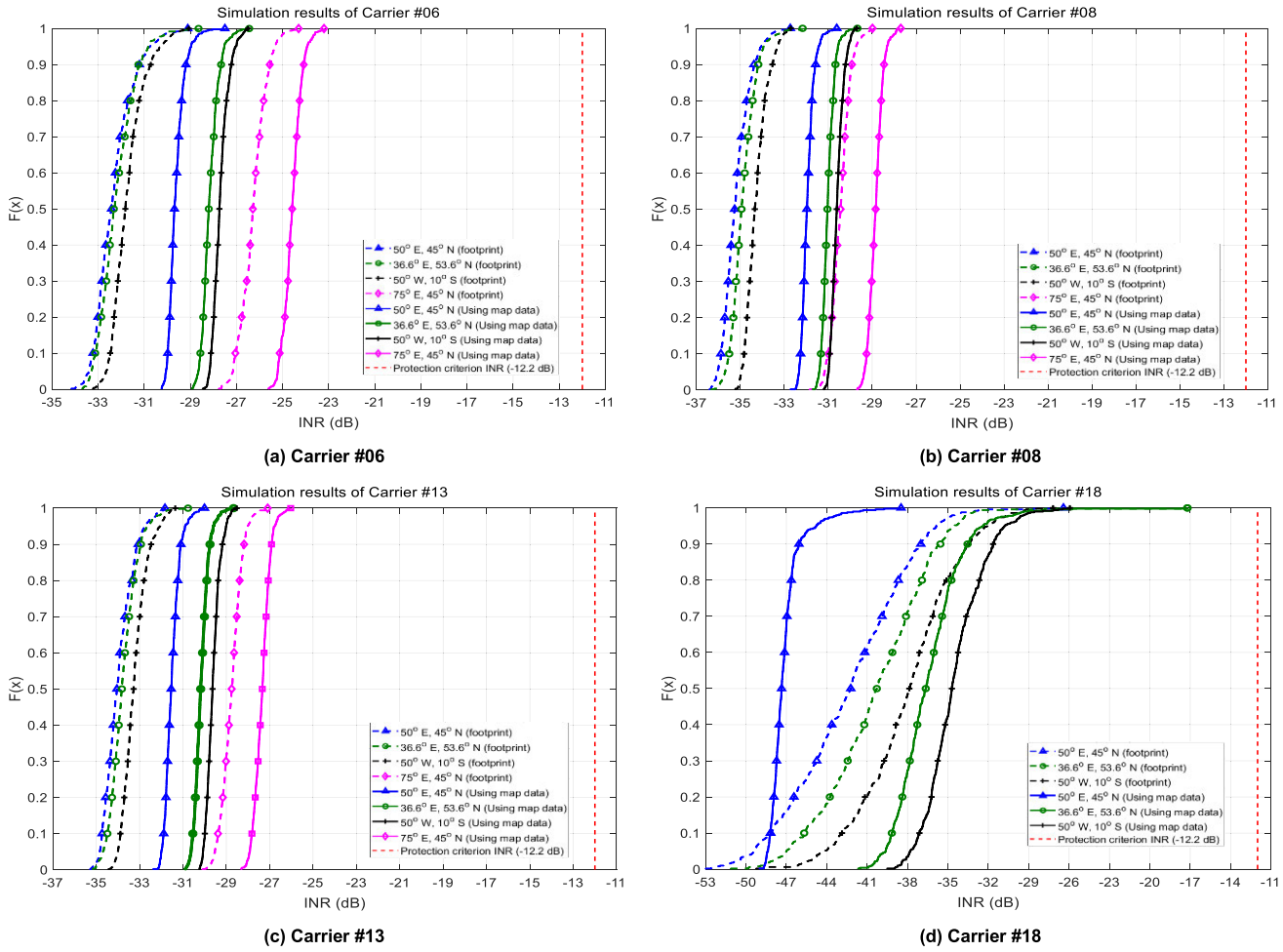

(a) Carrier #06 (b) Carrier #08

(c) Carrier #13 (d) Carrier #18

FIGURE 17. INR CDF of FSS satellites.

suburban, and urban areas. We take this into account and calculate the interference power that the passive sensor receives from the IMT-2020 when it scans the urban or suburban areas.

Fig. 14 shows the interference scenario when the passive sensor is aimed toward an urban area. The area within 1000 km^2 of the main beam position of the sensor is assumed to be an urban area and the remaining area is a suburban area. We set the residential area ratio R_b to 100% in the urban area and 5% in the suburban area [22].

Table 5 shows the parameters of the EESS passive sensor [37] and uses Tables 2 and 4 to calculate the interference power received by the passive sensor in the same way as is done in the FSS interference scenario. In this case, we assumed that the main beam directions of the sensor are directed toward Germany (6.88° E 50.5° N), the United Kingdom (2.3° W 53.23° N), and the coastlines of Korea (126.5° E, 34.5° N), respectively.

Because the EESS passive receives interference from the IMT-2020 located in the adjacent channel, when calculating P_t in (21), it calculates the transmitting power of the IMT-2020 that leaks into the frequency band of EESS passive, taking into account the unwanted emission mask of

TABLE 5. EESS passive sensor parameters [37].

Parameter [Unit]	Value	
Sensor number	F3	F5
Frequency [GHz]	23.8	
orbit altitude [km]	828	824
Antenna gain [dBi]	52	30.4
Main beam efficiency [%]	95	
Elevation angle [°]	34.8	26
Slant path distance [km]	1309.0	824.0
Antenna diameter [m]	2.06	0.17
−3dB beamwidth [°]	0.50	6.00
Protection criterion (dBm/200 MHz)	−166 dBm/200 MHz [38]	

IMT-2020. In this interference scenario, it is assumed that IMT-2020 is serviced in the 24.25–27.5 GHz band, where the unwanted emission level of IMT-2020 is shown in Table 5. In addition, G_{SS} in (21) refers to the gain of the receiving

antenna of the EESS passive sensor and is given as [39]

$$G_{ss}(\psi) = \begin{cases} G_{\max} - 1.8 \times 10^{-3} \left(\frac{D}{\lambda}\psi\right)^2, & \left(0^{\circ} \le \psi \le \psi_m\right) \\ \max(G_{\max} - 1.8 \times 10^{-3} \left(\frac{D}{\lambda}\psi\right)^2, & \\ -5\log\left(\frac{D}{\lambda}\right) - 25\log(\psi)), & \left(\psi_m < \psi \le 69^{\circ}\right) \\ -13 - 5\log\left(\frac{D}{\lambda}\right), & \left(69 < \psi \le 180^{\circ}\right), \end{cases} \tag{29}$$

where D and λ are the antenna diameter and wavelength [37].

Fig. 15 shows the antenna patterns of the sensors. Fig. 16 shows the antenna gain according to the sensor's main beam position. In Fig. 16, the sensors all have the same antenna gain distribution because they have the same elevation angle at all main beam positions. However, because the area removed by using the map data is different, the antenna gain distribution depends on the geographic coordinates that the sensor scans. In addition, EESS passive has a small coverage area because the EESS passive service operates at a lower altitude than the FSS satellite.

VI. SIMULATION RESULTS

Our simulation is basically based on a Monte Carlo simulation to consider the randomness of interference power. The cumulative interference power received by a satellite system is determined by various random variables such as the location, environment, antenna direction, and beamforming direction of the IMT-2020 (main beam of a BS points a desired UE, and vice versa). Therefore, whenever the simulation result is repeated obtained by repeating a snapshot of IMT-2020 network with randomness, the same scenario with the Monte Carlo simulation method, new random variables are set, and the a variation of the interference power received by satellite for each simulation snapshot is analyzed with regard to expressed as a cumulative distribution function (CDF). The simulation results are then compared to the protection criteria of each satellite system to suggest the possibility of coexistence between the IMT-2020 and the satellite system.

A. RESULTS OF FSS INTERFERENCE SCENARIO

Fig. 17 shows the simulation results of the FSS interference scenario. In this figure, the dotted line is the result of considering only the footprint that was used in the existing interference-analysis technique, and the solid line is the result considering only the land area in the entire coverage area by considering the satellite's side lobe and terrain data as proposed in this paper.

The simulation results show that for the main beam directed to (36.6° E 53.6° N), Carrier #06 in the 27-GHz band and Carrier #18 in the 81 GHz receives an additional interference up to 5.3 dB and 7.9 dB, respectively. This means that when calculating the interference received by satellites, not only the footprint but also the interference received from the side lobes must be considered for a more accurate calculation. In addition, the simulation results show that the interference power received by the satellite from the IMT-2020 depends on the main beam direction of the satellite. The lower the satellite's elevation angle, the more interference the satellite receives. The reason for this is that the lower the satellite's elevation angle, the larger the footprint, and the lower the elevation angle of the IMT-2020 distributed in the footprint, which increases the satellite's receiving antenna's gain and the IMT-2020's transmitting antenna's gain.

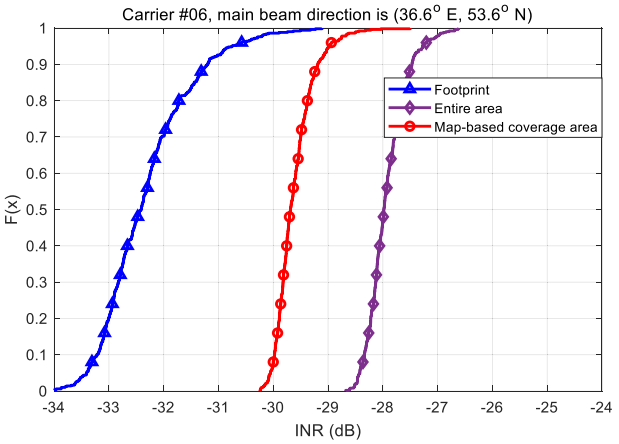

(a) Carrier #06, Main beam direction: (36.6° E, 53.6° N)

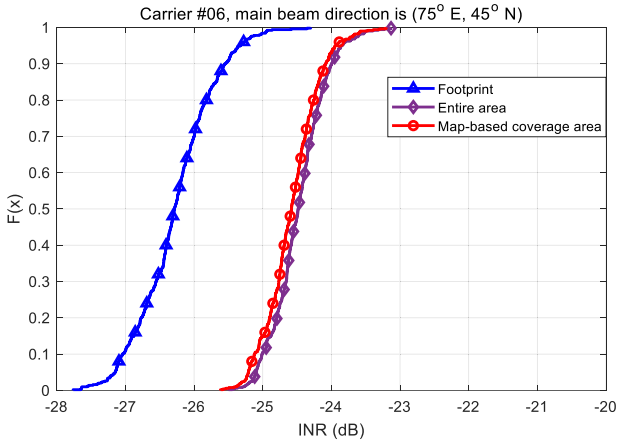

(b) Carrier #06, Main beam direction: (75° E, 45° N)

FIGURE 18. INR CDF of a FSS satellite for various interference-receiving area.

In addition, when the main beam is directed to (50° E, 45° N) in the Carrier #18 satellite, we can confirm that the resulting graph is different from the results of other main beam directions. The reason for this can be seen in Fig. 13. The antenna pattern of Carrier #18 in Fig. 13 has a lower orbit, narrower 3-dB beamwidth, and higher maximum antenna gain than do the other satellites. Thus, Carrier #18 satellites have a relatively narrower footprint than other satellites, and the maximum antenna gain is higher, resulting in a greater impact from interference received from the footprint. In Fig. 13(a), we can see that when the satellite's

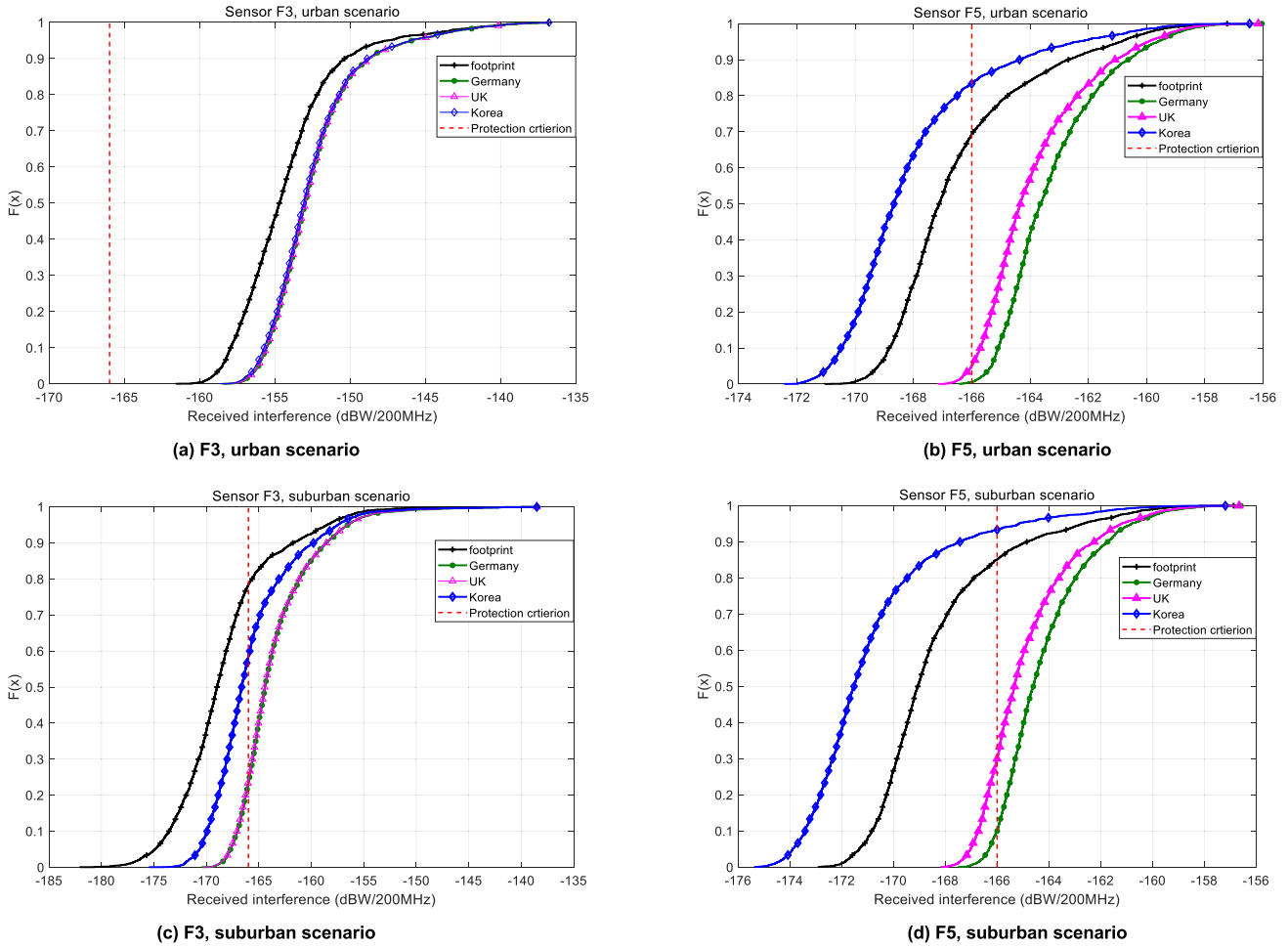

(a) F3, urban scenario

(b) F5, urban scenario

(c) F3, suburban scenario

(d) F5, suburban scenario

FIGURE 19. CDF of received interference power of the EESS passive sensors. (BS: 8 × 8, UE: 4 × 4).

main beam is facing (50° E, 45° N), the satellite's footprint is cut off by the Caspian Sea, which is located near the main beam location. Unlike other satellites, which cut off only a portion of the footprint, Carrier #18 satellites have a narrow footprint, so most footprints are excluded by the Caspian Sea. Therefore, when the main beam is directed at (50° E, 45° N) in Carrier #18, we can see that the interference is smaller than that with the method considering only the footprint using the interference-analysis model proposed in this paper.

If we put all the simulation results together, satellites in the 27-GHz band receive, on average, more interference than Carrier #18 satellite due to the large coverage area and footprint, and have a lower propagation loss when compared to Carrier #18 satellite. However, the Carrier #18 satellite is located in a low orbit, so it has a relatively low elevation angle if it has the same main beam direction as the other satellites. In addition, the antenna array of the IMT-2020 in the 81–86-GHz band is larger than the antenna array of the IMT-2020 in the 24.25–27.5-GHz band, increasing the transmitting antenna's gain of the IMT-2020. Therefore, in the worst case, Carrier #18 satellite may receive more interference than satellites in the 27-GHz band. Nevertheless, the interference received by satellite systems at both 27 GHz and 81 GHz satisfy the satellite's protection criteria of −12.2 dB. Therefore, even if the IMT-2020 is serviced in the same band, it can be seen that the FSS satellite is not significantly affected by the interference of the IMT-2020.

In addition, Fig. 18 shows the INR CDF of Carrier #6 satellite whose interference-receiving area is footprint, entire coverage area, and the proposed map-based coverage area, respectively. In Fig. 18, we performed the simulation under the same conditions for all conditions except the main beam direction of the satellite. In Fig. 18(a), the INR values are clearly different for each receiving area, but in Fig. 18 (b), there is no significant difference between the case of the entire coverage area and the map-based coverage area. The reason is that in Fig. 18(b), the map-based method removes only the area for which the receiving antenna gain of the satellite is low. Therefore, we confirm that a more accurate interference analysis is possible using the proposed map-based approach.

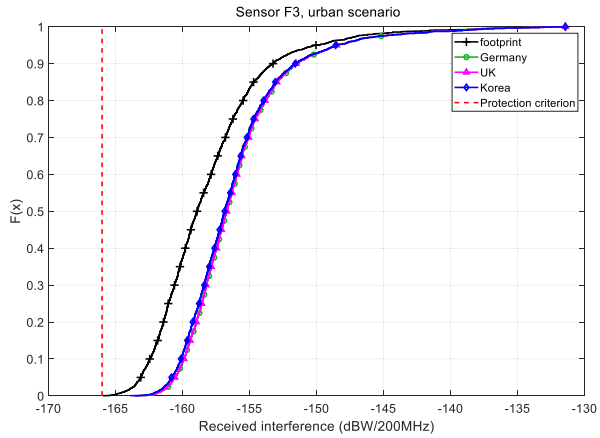

(a) F3, urban scenario

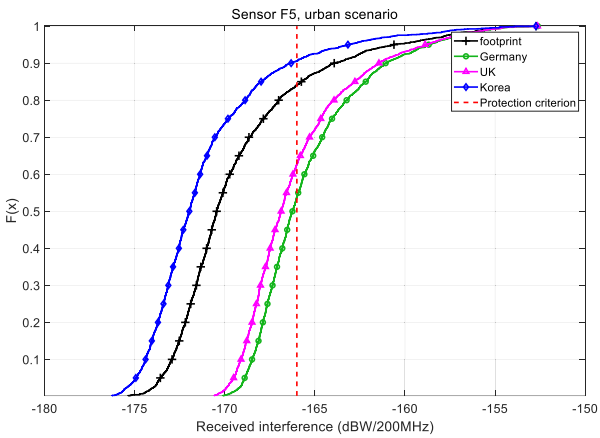

(b) F5, urban scenario

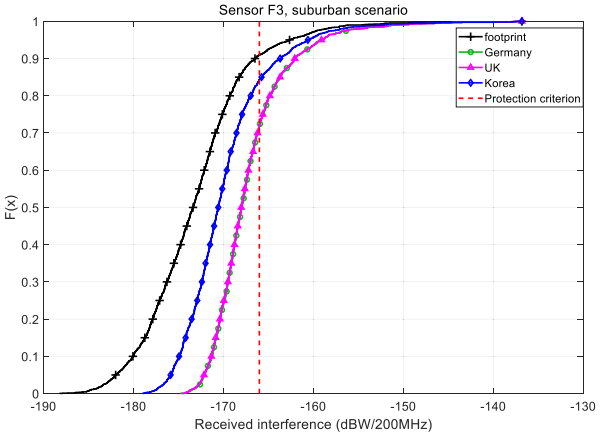

(c) F3, suburban scenario

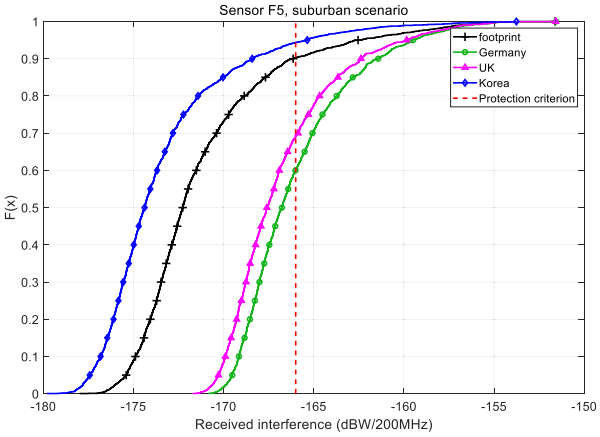

(d) F5, suburban scenario

FIGURE 20. CDF of received interference power of the EESS passive sensors. (BS: 16 × 16, UE: 8 × 8).

B. RESULTS OF EESS PASSIVE INTERFERENCE SCENARIO

Fig. 19 shows the simulation results of the EESS passive interference scenario. To illustrate the worst-case scenario, each sensor was assumed to have a minimum elevation angle. In Fig. 19, (a) and (b) show the interference power received when the main beam position of each sensor is in the urban area, and (c) and (d) show the interference power received when the main beam position of each sensor is in the suburban area.

As a result of the simulation, when the main beam position is directed toward Germany or the United Kingdom, the interference is increased compared to that only considering the footprint in all scenarios, because it receives interference from the side lobe as well as the footprint. However, if the main beam position is directed toward the coastline of Korea, sensors F3 and F5 show different results.

In the result of sensor F3, when the main beam position is pointed toward Korea, the interference power received by the sensor is higher than when only the footprint is taken into account. However, sensor F5 does the opposite. The reason for this is the difference in the antenna pattern of the sensor. Sensor F3 has a small footprint because of its narrow beamwidth. Therefore, even if the main beam position is facing the shoreline, most footprints remain and additional interference from side lobes is received, so it receives more interference power than the result that considers only the footprint. However, because sensor F5 has a wide beamwidth, the footprint is large. Therefore, when the main beam position faces the shoreline, most footprints are removed, resulting in a significant decrease in the interference power received by the sensor, which results in less interference than when the result of the footprint is considered.

Additionally, (c) and (d) in Fig. 19 show the interference power received by each sensor according to the main beam position when the main beam position of the sensor is pointed toward a suburban environment. In the suburban environment interference scenario, each sensor receives less interference than shown in (a) and (b) as a result of the urban environment scenario because the number of IMT-2020s deployed

within 1000 km of the main beam location decreases by 0.05 times compared to the urban environment. As a result of comparing the interference each sensor receives depending on the urban environment, sensor F3 receives an average of 13.6 dB and sensor F5 receives an average of 2.2 dB less interference. For sensor F3, the maximum antenna gain is high and the beam width is narrow. Thus, the interference received from the IMT-2020 placed inside the footprint accounts for a large part of the cumulative interference power. Therefore, the cumulative interference power received by sensor F3 varies greatly depending on the number of IMT-2020s in the footprint. However, sensor F5 has a large footprint due to its low antenna gain and wide beamwidth. Therefore, unlike sensor F3, sensor F5 has a small difference in the cumulative interference power received in urban and suburban environments. Table 5 shows the probability of meeting the protection criteria in each scenario using the results of each simulation. In all scenarios, EESS passive sensors have a high probability of failing to meet the protection criteria.

Fig. 20 shows the cumulative interference power received by the EESS passive sensor when the antenna array of BS and UE is increased to 16×16 and 8×8, respectively. When the number of antenna elements of the IMT-2020 increases, the beamforming pattern of the IMT-2020 has higher directivity and the side lobe gain decreases. Therefore, the interference received by the sensor in all scenarios is reduced because the transmit antenna gain in the direction of the sensor is reduced. However, in urban area, F3 sensors still do not meet the protection criteria in all scenarios, as shown in Fig. 20 (a), and in F5 sensors are 84.2% (footprint), 54.4% (Germany), 62.2% (UK), and 90.6% (Korea), respectively, for each scenario, as shown in Fig. 20 (b). In addition, if the EESS passive sensors scan the suburban area, the probability that the sensor F3 meets the protection criteria is 91%, 72%, 72%, and 84.3%, respectively, and the sensor F5 is 91.6%, 68%, 74.8%, and 95.3%, respectively. This satisfies the protection criteria with a higher probability than the previous results but does not guarantee the complete coexistence of IMT-2020 and EESS passive.

VII. CONCLUSION

In this work, we proposed an interference-analysis modeling method to check the coexistence of IMT-2020 and the existing satellite services in the mmWave band in relation to the IMT-2020 frequency-designation agenda. In addition, we performed interference analysis and presented the coexistence possibility of IMT-2020 and satellite services when IMT-2020 is operated in the candidate bands using the proposed methodology.

For accurate simulation, we modeled the IMT-2020 using the modeling document proposed by ITU and distributed the IMT-2020 with different environments in the entire coverage area. Subsequently, IMT-2020 was sampled in consideration of only the land area of the satellite's entire coverage area using map data, and interference analysis was performed in consideration of the various kinds of propagation losses occurring between the ground and space in the mmWave band. Then, we verified the possibility of coexistence compared with the protection criteria of each satellite system.

The simulation results show that the FSS satellite receives interference from many IMT-2020s because it is located at a high altitude. However, due to the high propagation loss and protection criteria, the operation of the FSS satellite is not affected, even when it operates in the same channel as the IMT-2020 in both the 27–27.5 and 81–86 GHz bands.

However, the EESS passive sensor is so sensitive that the low protection standards render it difficult to operate, even if the IMT-2020 is serviced in adjacent bands. In particular, when the main beam of the sensor is directed toward the urban area, the interference of most passive sensors exceeds the protection standard, which is a critical problem for the EESS passive service operations. Therefore, to ensure the coexistence of the two services, consideration should be given to reducing the interference power of the IMT-2020, such as additional frequency separation or interference mitigation techniques.

The proposed interference-analysis method is not limited to IMT-2020 and satellite systems, but can be extended to various interference scenarios such as terrestrial network services and aviation systems. Recently, satellite communication technology utilizing low-orbit satellites has been developing rapidly, and LEO satellite-based mobile communication services are expected to become common in 6th-generation mobile communication. Our study can be applied to research related to the construction of the ground-space integrated communication network.

REFERENCES

[1] Cisco. (2017). *Cisco Visual Networking Index (VNI) Update Global Mobile Data Traffic Forecast 2016-2021*. Accessed: May 10, 2020. [Online]. Available: http://www.usuariosdigitales.org/wp-content/uploads/2017/02/mobile-white-paper-c11-520862-1.pdf

[2] T. S. Rappaport, S. Sun, R. Mayzus, H. Zhao, Y. Azar, K. Wang, G. N. Wong, J. K. Schulz, M. Samimi, and F. Gutierrez, "Millimeter wave mobile communications for 5G cellular: It will work!" *IEEE Access*, vol. 1, pp. 335–349, 2013.

[3] A. Bleicher, "The 5G phone future," *IEEE Spectr.*, vol. 50, no. 7, pp. 15–16, Jul. 2013.

[4] *Final Acts WRC-15 World Radiocommunication Conference*, document ITU-R, 2015, [Online]. Available: https://www.itu.int/pub/R-ACT-WRC.12-2015/en

[5] *Liaison Statement to Task Group 5/1—Spectrum Needs and Characteristics for the Terrestrial Component of IMT in the Frequency Range between 24.25 GHz and 86 GHz*, document ITU-R TG5.1 Contribution 36, 2017. Accessed: May 10, 2020. [Online]. Available: https://www.itu.int/md/R15-TG5.1-C-0036/en

[6] *Modelling and Simulation of IMT Networks and Systems for Use in Sharing and Compatibility Studies*, document ITU-R M.2101-0, 2017. Accessed: May 10, 2020. [Online]. Available: https://www.itu.int/rec/R-REC-M.2101/en

[7] W. A. Hassan, H.-S. Jo, and A. R. Tharek, "The feasibility of coexistence between 5G and existing services in the IMT-2020 candidate bands in Malaysia," *IEEE Access*, vol. 5, pp. 14867–14888, 2017.

[8] G. Hattab, E. Visotsky, M. Cudak, and A. Ghosh, "Coexistence of 5G mmWave users with incumbent fixed stations over 70 and 80 GHz," in *Proc. IEEE Globecom Workshops (GC Wkshps)*, Singapore, Dec. 2017, pp. 1–5.

[9] W. A. Hassan, H.-S. Jo, S. Ikki, and M. Nekovee, "Spectrum-sharing method for co-existence between 5G OFDM-based system and fixed service," *IEEE Access*, vol. 7, pp. 77460–77475, 2019.

[10] J. Kim, L. Xian, and A. S. Sadri, "Numerical simulation study for frequency sharing between micro-cellular systems and fixed service systems in millimeter-wave bands," *IEEE Access*, vol. 4, pp. 9847–9859, 2016.

[11] J. Park, E. Lee, S.-H. Park, S.-S. Raymond, S. Pyo, and H.-S. Jo, "Modeling and analysis on radio interference of OFDM waveforms for coexistence study," *IEEE Access*, vol. 7, pp. 35132–35147, 2019.

[12] J.-W. Lim, H.-S. Jo, H.-G. Yoon, and J.-G. Yook, "Interference mitigation technique for the sharing between IMT-advanced and fixed satellite service," *J. Commun. Netw.*, vol. 9, no. 2, pp. 159–166, Jun. 2007.

[13] F. Guidolin and M. Nekovee, "Investigating spectrum sharing between 5G millimeter wave networks and fixed satellite systems," in *Proc. IEEE Globecom Workshops (GC Wkshps)*, San Diego, CA, USA, Dec. 2015, pp. 1–7.

[14] J. Chen, Z. Qian, T. Wang, and X. Li, "Analysis on the protection distance for spectrum sharing between IMT-2020(5G) and EESS systems in 25.5–27 GHz band," in *Proc. IEEE 2nd Inf. Technol., Netw., Electron. Autom. Control Conf. (ITNEC)*, Chengdu, China, Dec. 2017, pp. 970–975.

[15] H. Tan, Y. Liu, Z. Feng, and Q. Zhang, "Coexistence analysis between 5G system and fixed-satellite service in 3400–3600 MHz," *China Commun.*, vol. 15, no. 11, pp. 25–32, Nov. 2018.

[16] H.-K. Son and Y.-J. Chong, "Coexistence of 5G system with fixed satellite service Earth station in the 3.8 GHz band," in *Proc. Int. Conf. Inf. Commun. Technol. Converg. (ICTC)*, Jeju, South Korea, Oct. 2018, pp. 1070–1073.

[17] F. Guidolin, M. Nekovee, L. Badia, and M. Zorzi, "A study on the coexistence of fixed satellite service and cellular networks in a mmWave scenario," in *Proc. IEEE Int. Conf. Commun. (ICC)*, London, U.K., Jun. 2015, pp. 2444–2449.

[18] T. Wang, Z. Qian, L. Kang, S. Geng, and X. Zhao, "Coexistence interference analysis of 28 GHz IMT and fixed-satellite service systems," in *Proc. IEEE 2nd Adv. Inf. Technol., Electron. Autom. Control Conf. (IAEAC)*, Chongqing, China, Mar. 2017, pp. 1574–1578.

[19] S. Kim, E. Visotsky, P. Moorut, K. Bechta, A. Ghosh, and C. Dietrich, "Coexistence of 5G with the incumbents in the 28 and 70 GHz bands," *IEEE J. Sel. Areas Commun.*, vol. 35, no. 6, pp. 1254–1268, Jun. 2017.

[20] Y. Cho, H. Kim, E. E. Ahiagbe, and H.-S. Jo, "Spectral coexistence of IMT-2020 with fixed-satellite service in the 27-27.5 GHz band," in *Proc. Int. Conf. Inf. Commun. Technol. Converg. (ICTC)*, Jeju, South Korea, Oct. 2018, pp. 1–6.

[21] Y. Cho, H.-K. Kim, and H.-S. Jo, "Coexistence between 5G mobile communication and fixed-satellite service in the millimeter wave band," *J. Korean Inst. Electromagn. Eng. Sci.*, vol. 30, no. 9, pp. 742–753, Sep. 2019.

[22] Y. Cho, H. Kim, D. K. Tettey, K.-J. Lee, and H.-S. Jo, "Modeling method for interference analysis between IMT-2020 and satellite in the mmWave band," in *Proc. IEEE Globecom Workshops (GC Wkshps)*, Waikoloa, HI, USA, Dec. 2019, pp. 1–6.

[23] *System Parameters and Propagation Models to be Used in Sharing and Compatibility Studies, ITU Reports Annex 01*. Accessed: May 10, 2020. [Online]. Available: https://www.itu.int/md/R15-TG5.1-C-0478/en

[24] *Water Vapour: Surface Density and Total Columnar Content*, document ITU-R P.836-6, 2017. Accessed: May 10, 2020. [Online]. Available: https://www.itu.int/rec/R-REC-P.836/en

[25] *Guide to the Application of the Propagation Methods of Radiocommunication Study Group 3*, document ITU-R P.1144-10, 2019. Accessed: May 10, 2020. [Online]. Available: https://www.itu.int/rec/R-REC-P.1144/en

[26] *Prediction of Clutter Loss*, document ITU-R P.2108-0, 2017. Accessed: May 10, 2020. [Online]. Available: https://www.itu.int/rec/R-REC-P.2108/en

[27] *Prediction of Building Entry Loss*, document ITU-R P.2109-0, 2019. Accessed: May 10, 2020. [Online]. Available: https://www.itu.int/rec/R-REC-P.2109/en

[28] *Propagation Data Required for the Evaluation of Interference between Stations in Space and Those on the Surface of the Earth*, document ITU-R P.619-4, 2019. Accessed: May 10, 2020. [Online]. Available: https://www.itu.int/rec/R-REC-P.619/en

[29] *Compilation of Measurement Data Relating to Building Entry Loss*, document ITU-R P.2346-3, 2019. Accessed: May 10, 2020. [Online]. Available: https://www.itu.int/pub/R-REP-P.2346-3-2019.

[30] *Study on Channel Model for Frequency Spectrum Above 6 GHz*, Release 14, document TR 38.900 V14.1.0, 3GPP, 2016. Accessed: May 10, 2020. [Online]. Available: http://www.3gpp.org/ DynaReport/38900.htm

[31] J. Pahl, "The interference calculation," in *Interference Analysis: Modelling Radio Systems for Spectrum Management*. Hoboken, NJ, USA: Wiley, 2016, pp. 217–327.

[32] S.-S. Raymond, A. Abubakari, H.-S. Jo, H.-J. Hong, and H. K. Son, "Compatibility between LTE and airport surveillance radar in 2700–2900 MHz radar bands," in *Proc. Int. Conf. Inf. Commun. Technol. Converg. (ICTC)*, Jeju, South Korea, Oct. 2015, pp. 1037–1042.

[33] ITU Reports. *FSS Technical Parameters for Sharing Studies Under WRC-19 Agenda Item 1.13 and 1.14*. Accessed: May 10, 2020. [Online]. Available: https://www.itu.int/md/R15-WP4A-C-0504/en

[34] *Satellite Antenna Radiation Pattern for Use as a Design Objective in the Fixed-Satellite Service Employing Geostationary Satellites*, document ITU-R P.619-4, 1997. Accessed: May 10, 2020. [Online]. Available: https://www.itu.int/rec/R-REC-S.672/en

[35] ITU Reports. *Protection Criteria and Apportionment for FSS Receivers for Use in Sharing Studies Under WRC-19 Agenda Item 1.13*. Accessed: May 10, 2020. [Online]. Available: https://www.itu.int/md/R15-WP4A-C-0644/en

[36] J. Zuzek. (2009). *Earth Exploration-Satellite Service (EESS)—Passive Spaceborne Remote Sensing*. Accessed: May 10, 2020. [Online]. Available: https://www.itu.int/dms_pub/itu-r/md/09/sem.wmo/c/R09-SEM.WMO-C-0010!!PDF-E.pdf

[37] *Typical Technical and Operational Characteristics of Earth Exploration? Satellite Service (passive) Systems Using Allocations between 1.4 and 275 GHz*, document ITU-R RS.1861-0, 2010. Accessed: May 10, 2020. [Online]. Available: https://www.itu.int/rec/R-REC-RS.1861/en

[38] *Performance and Interference Criteria for Satellite Passive Remote Sensing*, document ITU-R RS.2017-0, 2012. Accessed: May 10, 2020. [Online]. Available: https://www.itu.int/rec/R-REC-RS.2017/en

[39] *Reference Antenna Pattern for Passive Sensors Operating in the Earth Exploration Satellite Service (Passive) to be Used in Compatibility Analyses in the Frequency Range 1.4-100 GHz*, document ITU-R RS.1813-1, 2011. Accessed: May 10, 2020. [Online]. Available: https://www.itu.int/rec/R-REC-RS.1813/en

YEONGI CHO (Student Member, IEEE) received the B.S. and M.S. degrees in electronics and control engineering from Hanbat National University, Daejeon, South Korea, in 2018 and 2020, respectively, where he is currently pursuing the Ph.D. degree with the Department of Electronics and Control Engineering. His current research interests are interference analysis between wireless cellular and satellite service and wireless communication system structure (physical layer, channel modeling).

HYUN-KI KIM (Student Member, IEEE) received the B.S. and M.S. degrees in electronics and control engineering from Hanbat National University, Daejeon, South Korea, in 2018 and 2020, respectively. His current research interests are spectral compatibility/coexistence and interference mitigation technique.

MAZIAR NEKOVEE received the Ph.D. degree in physics from the University of Nijmegen, The Netherlands, and a first degree *(cum laude)* in electrical and electronic engineering from the Delft University of Technology, The Netherlands. In 2017, he was a Chief Engineer and the Head of 5G Research and European Collaborations at Samsung R&D UK. Prior to that, he was with British Telecom (BT) Research and Technology as a Senior Scientist, and subsequently the Team Leader. He is currently a Professor of telecoms and mobile technology and also the Head of the Centre for Advanced Communication, Mobile Technology, and IoT, School of Engineering and Informatics, University of Sussex, U.K. His research interests and expertise include 5G and beyond-5G/6G mobile communication RAN and Core design, machine-learning and AI applied to communication networks, spectrum sharing, cognitive radio, millimeter-wave, and THz communications. He has authored over 120 highly cited peer-reviewed papers, one best-selling book "*Cognitive Radio Communications and Networks: Principle and Practice*" and holds 13 family of patents in telecommunication and mobile technologies. He is a sought-after speaker at high-level industry events, C-level meetings with European operators, policymakers, and at international conferences. He is the recipient of a number of industry and academic awards, including a Royal Society (UK Academy of Science) Industry Fellowship, BT Innovation Award, and Samsung's Best Practice of Research Award.

HAN-SHIN JO (Member, IEEE) received the B.S., M.S., and Ph.D. degrees in electrical and electronics engineering from Yonsei University, Seoul, South Korea, in 2001, 2004, and 2009, respectively.

He was a Postdoctoral Research Fellow with the Wireless Network and Communications Group, Department of Electrical and Computer Engineering, University of Texas at Austin, from 2009 to 2011. He developed a long-term evolution base station in Samsung Electronics from 2011 to 2012. He is currently an Associate Professor with the Department of Electronics and Control Engineering, Hanbat National University, Daejeon, South Korea. His current research interests are in all the aspects of MIMO (channel modeling, precoding, and scheduling with limited feedback, beamforming, SDMA, and massive MIMO) and applications of stochastic geometry and optimization theory to wireless cellular and ad hoc networks. He was a recipient of the Samsung Electronics Graduate Fellowship from 2006 to 2008, the Korea Research Foundation BrainKorea21 Graduate Fellowship from 2006 to 2007, the Korea Research Foundation Post-Doctoral Fellowship in 2009, and the 2011 ETRI Journal Best Paper Award.